Influence of fault rock foliation on fault zone permeability: The case of deeply buried arkosic sandstones (Gres d'Annot, southeastern France)

Thibault Cavailhes, Jean-Pierre Sizun, Pierre Labaume, Alain Chauvet, Martine Buatier, Roger Soliva, Leila Mezri, Delphine Charpentier, Henri Leclere, Anna Trave, et al.

Influence of fault rock foliation on fault zone permeability: The case of deeply buried arkosic sandstones (Grès d'Annot, southeastern France)

Thibault Cavailhes, Jean-Pierre Sizun, Pierre Labaume, Alain Chauvet, Martine Buatier, Roger Soliva, Leila Mezri, Delphine Charpentier, Henri Leclère, Anna Travé, and Claude Gout

ABSTRACT

We describe the structure, microstructure, and petrophysical properties of fault rocks from two normal fault zones formed in low-porosity turbiditic arkosic sandstones, in deep diagenesis conditions similar to those of deeply buried reservoirs. These fault rocks are characterized by a foliated fabric and quartz-calcite sealed veins, which formation resulted from the combination of the (1) pressure solution of quartz, (2) intense fracturing sealed by quartz and calcite cements, and (3) neoformation of synkinematic white micas derived from the alteration of feldspars and chlorite. Fluid inclusion microthermometry in quartz and calcite cements demonstrates fault activity at temperatures of 195°C to 268°C. Permeability measurements on plugs oriented parallel with the principal axes of the finite strain ellipsoid show that the Y axis (parallel with the foliation and veins) is the direction of highest permeability in the foliated sandstone (10^{-2} md for Y against 10^{-3} md for X, Z, and the protolith, measured at a confining pressure of 20 bars). Microstructural observations document the localization of the preferential fluid path between the phyllosilicate particles forming the foliation. Hence, the direction of highest permeability in these fault rocks would be parallel with the fault and subhorizontal, that is, perpendicular to the slickenlines representing the local slip direction on the fault surface. We suggest

AUTHORS

THIBAULT CAVAILHES ~ *Géosciences Montpellier, unité mixte de recherche 5243, Université Montpellier 2-Centre National de la Recherche Scientifique, Place Eugène Bataillon, 34095 Montpellier Cedex 5, France; present address: Badley Ashton & Associates Ltd., Winceby, United Kingdom; thibaultcavailhes@badley-ashton.co.uk*

Thibault Cavailhes received his Ph.D. in 2012 from the Université de Montpellier 2 and now works for Badley Ashton. His area of interest includes fracturing and faulting mechanisms and their relationships with diagenetic context.

JEAN-PIERRE SIZUN ~ *Chrono-Environnement, unité mixte de recherche 6249, Université de Franche-Comté-Centre National de la Recherche Scientifique, 16 Route de Gray, 25030 Besançon Cedex, France; jpsizun@univ-fcomte.fr*

Jean-Pierre Sizun received his Ph.D. in 1995 from the University of Strasbourg. Since 1997, he has been an assistant professor at the Université de Franche-Comté. His research focuses on pore structures of rocks and their relationships with transfer properties in various geologic contexts.

PIERRE LABAUME ~ *Géosciences Montpellier, unité mixte de recherche 5243, Université Montpellier 2-Centre National de la Recherche Scientifique, Place Eugène Bataillon, 34095 Montpellier Cedex 5, France; pierre.labaume@gm.univ-montp2.fr*

Pierre Labaume received his Ph.D. in 1983 from the Université de Montpellier 2. Since 1983, he has been working as a researcher for the Centre National de la Recherche Scientifique in Montpellier and Grenoble universities. His research concerns mainly basin and thrust belt tectonics and fault structure.

ALAIN CHAUVET ~ *Géosciences Montpellier, unité mixte de recherche 5243, Université Montpellier 2-Centre National de la Recherche Scientifique, Place Eugène Bataillon, 34095 Montpellier Cedex 5, France; alain.chauvet@gm.univ-montp2.fr*

Alain Chauvet received his Ph.D. in 1989 from the Université de Montpellier 2. Since 1989, he has been working as a researcher for the Centre National de la Recherche Scientifique in Orléans and Montpellier universities. Most of his research is focused on the relationships between fluid and deformation, in particular, the mode of formation of mineral resources.

Martine Buatier ~ *Chrono-Environnement, unité mixte de recherche 6249, Université de Franche-Comté-Centre National de la Recherche Scientifique, 16 Route de Gray, 25030 Besançon Cedex, France; martine.buatier@univ-fcomte.fr*

Martine Buatier received her Ph.D. in 1989 from the Université de Strasbourg. After a postdoctoral position at the University of Michigan, Ann Arbor, she became an assistant professor at the Université de Lille, France in 1990. Since 1998, she has been a professor at the Université de Franche-Comté. Her research interests include fluid-sediment interactions and mineralogy of clays in hydrothermal, diagenetic, and fault zone environments.

Roger Soliva ~ *Géosciences Montpellier, unité mixte de recherche 5243, Université Montpellier 2-Centre National de la Recherche Scientifique, Place Eugène Bataillon, 34095 Montpellier Cedex 5, France; roger.soliva@gm.univ-montp2.fr*

Roger Soliva received his Ph.D. in 2004 from the Université de Paris-Sud. After a postdoctoral position at the University of Nevada, Reno, he became an assistant professor at the Université de Montpellier 2 in 2005. His research interests include fault growth, deformation bands, rupture mechanics, and tectonics in general.

Leila Mezri ~ *Géosciences Montpellier, unité mixte de recherche 5243, Université Montpellier 2-Centre National de la Recherche Scientifique, Place Eugène Bataillon, 34095 Montpellier Cedex 5, France; leilamezri@yahoo.fr*

Leila Mezri is preparing a Ph.D. on the numerical modeling of orogens at the Universite de Pierre et Marie Curie, Paris. She worked at the Laboratoire Geosciences Montpellier during summer of 2011 doing research on fluid inclusions in the Grès d' Annot.

Delphine Charpentier ~ *Chrono-Environnement, unité mixte de recherche 6249, Université de Franche-Comté-Centre National de la Recherche Scientifique, 16 Route de Gray, 25030 Besançon Cedex, France; Delphine.Charpentier@univ-fcomte.fr*

Delphine Charpentier received her Ph.D. in 2001 from the Université de Nancy. After postdoctoral positions at the Toulouse, Nancy, and Liverpool universities, she became an assistant professor at the Université de Franche-Comté in 2005. Her research concerns fluid-sediment interactions, in particular, the study of mass transfers and mineralogical changes in fault zones coupling high-resolution mineralogical characterization and geochemical modeling.

that a similar relationship between kinematic markers and fault rock permeability anisotropy may be found in other fault zone types (reverse or strike-slip) affecting feldspar-rich lithologies in deep diagenesis conditions.

INTRODUCTION

Fault zones are one of the main structures responsible for partitioning sedimentary basins and geologic reservoirs (Corrigan, 1993; Fisher et al., 2001). Understanding and predicting their function in fluid migration is thus an important issue in predicting reservoir quality. Parameters controlling this function involve the permeability and thickness of the fault rock, the type of fluid permeating through it, the pressure difference across the fault, and the considered time scale (e.g., Faulkner and Rutter, 1998).

In the last four decades, numerous works have focused on faulting mechanisms in high-porosity sandstones at shallow crustal depth (Aydin, 1978; Antonellini and Aydin, 1994; Fossen et al., 2007) and their influence on fluid flow (Eichhubl et al., 2004; Fossen and Bale, 2007). Typical structures described by these studies are deformation bands, where grain-to-grain movements and intragranular fracturing (cataclasis) are the main deformation mechanisms (Fossen et al., 2007). With the exception of some works that document a potential capillarity effect of cataclastic deformation bands (Sigda and Wilson, 2003; Cavailhes et al., 2009), the literature generally describes a permeability reduction in these structures from 1 to 6 orders of magnitude relative to the host rock (e.g., Fossen et al., 2007). By contrast, relations between faulting and fluid flow in low-porosity sandstones buried to deep diagenesis conditions (150–250°C) have been much less studied (Fisher et al., 2003; Surma et al., 2003; Balsamo et al., 2010; Laubach et al., 2010). In these conditions, which are those of the deeply buried reservoirs, in particular, the tight-gas sandstones, mechanical and chemical processes are intimately linked in faulting mechanisms. Some studies have investigated the influence on fluid flow of fracture opening and sealing in deeply buried sandstones (e.g., Laubach and Ward, 2006; Ward et al., 2006; Olson et al., 2009), but little attention has been paid to the hydraulic behavior of foliation, which can develop in specific lithologies in deep settings.

This article describes the relationships between foliated fault rock structure, microstructure, and permeability in normal fault zones with tens-of-meters of offsets affecting low-porosity, deeply buried, turbiditic sandstones of arkosic composition. We emphasize the function of the feldspath-rich lithology in

foliation development at high temperature and apply a novel methodology of petrophysical measurement orientation to quantify foliated fault rock permeability. To assess the function of the structural heterogeneities, that is, veins and foliation, in permeability anisotropy, we measure the matrix porosity and permeability along the principal axes (X, Y, and Z) of the strain ellipsoid and compare them with the host rock values. From these data, we define the shape ratio of the permeability ellipsoid and its orientation with respect to fault rock foliation. We discuss the implications of these results on the function of foliated fault zones as either conduit or barrier to fluid flow.

GEOLOGIC SETTING

The studied faults affect the Grès d'Annot Formation, in the southwestern Alps external zone (Figure 1A). The Grès d'Annot Formation corresponds to a Priabonian–Rupelian arkosic turbidite succession mainly sourced from the Variscan crystalline basement of the Corsica-Sardinia massif and deposited in the Alpine foreland basin (Joseph and Lomas, 2004). The Grès d'Annot Formation caps the Mesozoic–Paleogene succession of the Digne Nappe and was buried below the Embrunais–Ubaye nappes during the late Oligocene–earliest Miocene (Kerckhove, 1969; Fry, 1989; Corsini et al., 2004; Labaume et al., 2008). Above the Grès d'Annot, the Schistes à Blocs Formation corresponds to an olistrostrome precursor of the Embrunais–Ubaye nappes (Kerckhove, 1969). In the study area, the nappe thickness was estimated at 8 to 10 km (5–6 mi), based on the 240°C to 260°C maximum temperature reached by the Grès d'Annot. These values are deduced from vitrinite reflectance, assuming a mean geothermal gradient of 25°C to 30°C/km (Labaume et al., 2009). During the Miocene, basement thrusting uplifted the Argentera and Barrot massifs (Bigot-Cormier et al., 2006; Sanchez, 2010), and related erosion resulted in the exhumation of the Grès d'Annot (Labaume et al., 2008).

The Grès d'Annot is cut by normal faults grouped in two families, transverse (around east–west) and longitudinal (north–south to north-northwest–south-southeast) to the belt (Kerckhove, 1969). The main faults of both families cut the whole structural system, from the Embrunais-Ubaye nappes down to the Paleozoic basement. Labaume et al. (1989) showed that the transverse faults predate the longitudinal faults and interpreted both families as post-nappe deformation, resulting from the gravitational collapse of the belt in the case of the

HENRI LECLÈRE ~ *Chrono-Environnement, unité mixte de recherche 6249, Université de Franche-Comté-Centre National de la Recherche Scientifique, 16 Route de Gray, 25030 Besançon Cedex, France; henri.leclere@univ-fcomte.fr*

Henri Leclère obtained his Ph.D. in 2012 from the Université de Franche-Comté. His research interests are focused on the mechanics of faults and earthquakes by combining geologic observations, laboratory experiments, and numerical modeling.

ANNA TRAVÉ ~ *Departament de Geoquimica, Petrologia i Prospeccio Geologica, Universitat de Barcelona, c/Marti i Franquès s/n, 08028 Barcelona, Spain; atrave@ub.edu*

Anna Travé received her Ph.D. from the Universitat de Barcelona in 1992. She is a professor at the University of Barcelona. Her research focuses on the relationships between fractures and fluid flow in compressive and extensional basins.

CLAUDE GOUT ~ *Total, Jean Feger Scientific and Technical Center, Avenue Larribau, 64018 Pau, France; claude.gout@total.com*

Claude Gout is a senior geologist for Total. He received his Ph.D. in 1987 from the Université de Grenoble. Since 1988, he has worked for Elf then Total, successively, as a structural geologist, an exploration geologist, and a reservoir geologist dealing with research and development geomodeling technologies as well as operational assets in the North Sea, Italy, and the Middle East. He currently manages and coordinates research and development projects about faults from reservoir to basin scale.

ACKNOWLEDGEMENTS

We thank TOTAL for financial support and the Parc National du Mercantour for sampling permit. T. Rossi and O. Chailan are acknowledged for their suggestions on an early draft of the manuscript. We thank A. P. Morris, C. Hermanrud, A. A. Kitchka, two anonymous reviewers, and S. E. Laubach, AAPG Editor, for their constructive reviews, which greatly contributed to the improvement of the paper.

The AAPG Editor thanks the following reviewers for their work on this paper: Christian Hermanrud, Alexander A. Kitchka, Alan P. Morris, and two anonymous reviewers.

EDITOR'S NOTE

Color versions of Figures 1–6 can be seen in the online version of this paper.

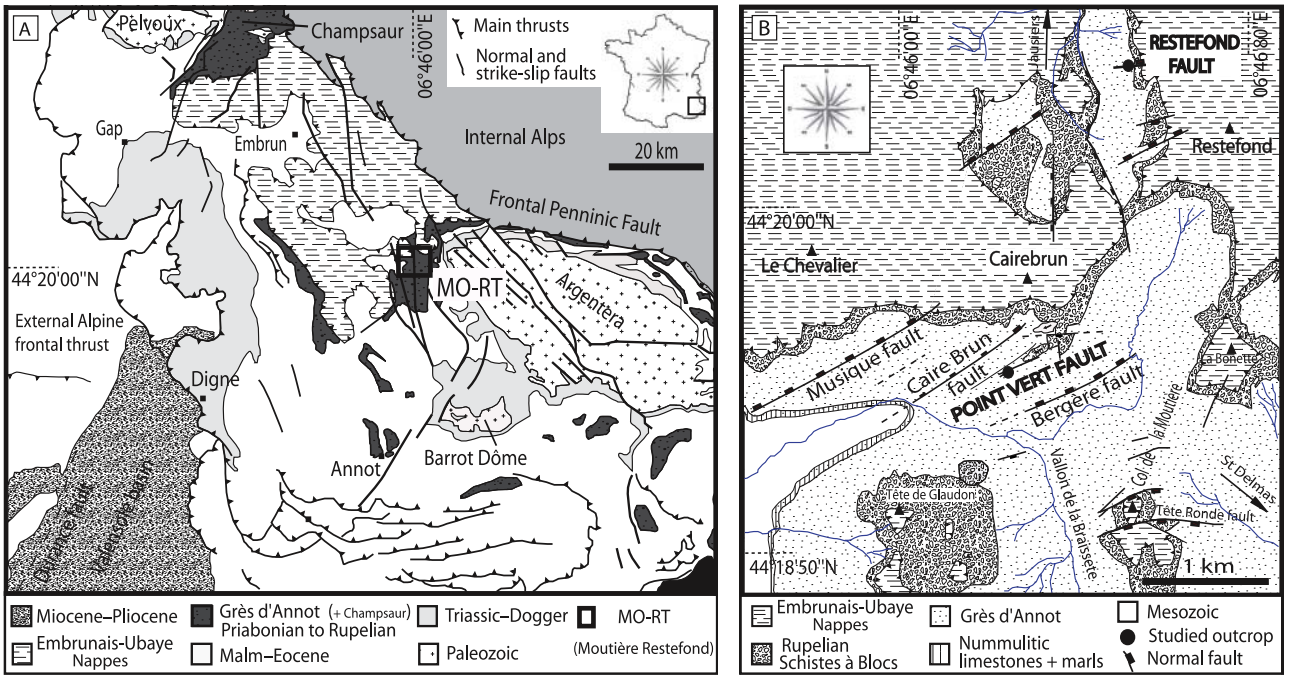

Figure 1. (A) Structural sketch map of the southwestern French Alps. The study area (Moutière-Restefond) is labeled MO-RT. (B) Structural sketch map of the study area, with the location of the studied Restefond and Point Vert fault outcrops.

longitudinal faults. More recently, some of the transverse faults were interpreted as contemporaneous to the Grès d'Annot and/or Schistes à Blocs by Bouroullec et al. (2004) and Pochat and van den Driessche (2007). Nevertheless, other recent studies demonstrate that the microstructures observed in these transverse fault zones are coherent with a fault activity at temperatures approximately 200°C (Du Bernard-Rochy, 2002; Leclère et al., 2012), that is, close to the maximum burial of the Grès d'Annot in the area (Labaume et al., 2009).

In this work, we study two east–west normal faults with tens of meters of throw that affect the Grès d'Annot Formation in the Moutière-Restefond area: the Restefond fault and the Point Vert fault (Figure 1B). They belong to a set of normal faults transverse to the belt with as much as 250-m (820-ft) displacement, which affect the Grès d'Annot, the Schistes à Blocs, and the Embrunais-Ubaye nappes. The Point Vert fault belongs to the fault set interpreted as synsedimentary by Bouroullec et al. (2004), whereas Leclère et al. (2012) show that the Restefond fault was active at temperatures approximately 200°C. We have determined from a field survey that the fault rock type described in this article for these two faults is representative of all the east–west faults present in the Moutière-Restefond area (~8 km [5 mi] east–west and 4 km [2 mi] north–south).

FAULT ZONE STRUCTURE

Restefond Fault Zone Structure

The Restefond fault cuts a subhorizontal turbidite succession composed of as much as several-meters-thick arkosic sandstone beds with as much as 1-m (3-ft)–thick pelitic intercalations (Du Bernard-Rochy, 2002; Leclère et al., 2012). The main fault surface trends approximately N080E and dips about 70° northward (Figure 2). The displacement cannot be measured precisely because of outcrop conditions but is estimated at approximately 15 m (49 ft).

On the studied transect, the hanging wall consists of a 10-m (33-ft)–thick bed of coarse to microconglomeratic sandstone, whereas the footwall is composed of slumped sandstone layers containing as much as 1 m (3 ft) of pelite lenses (Figure 2A).

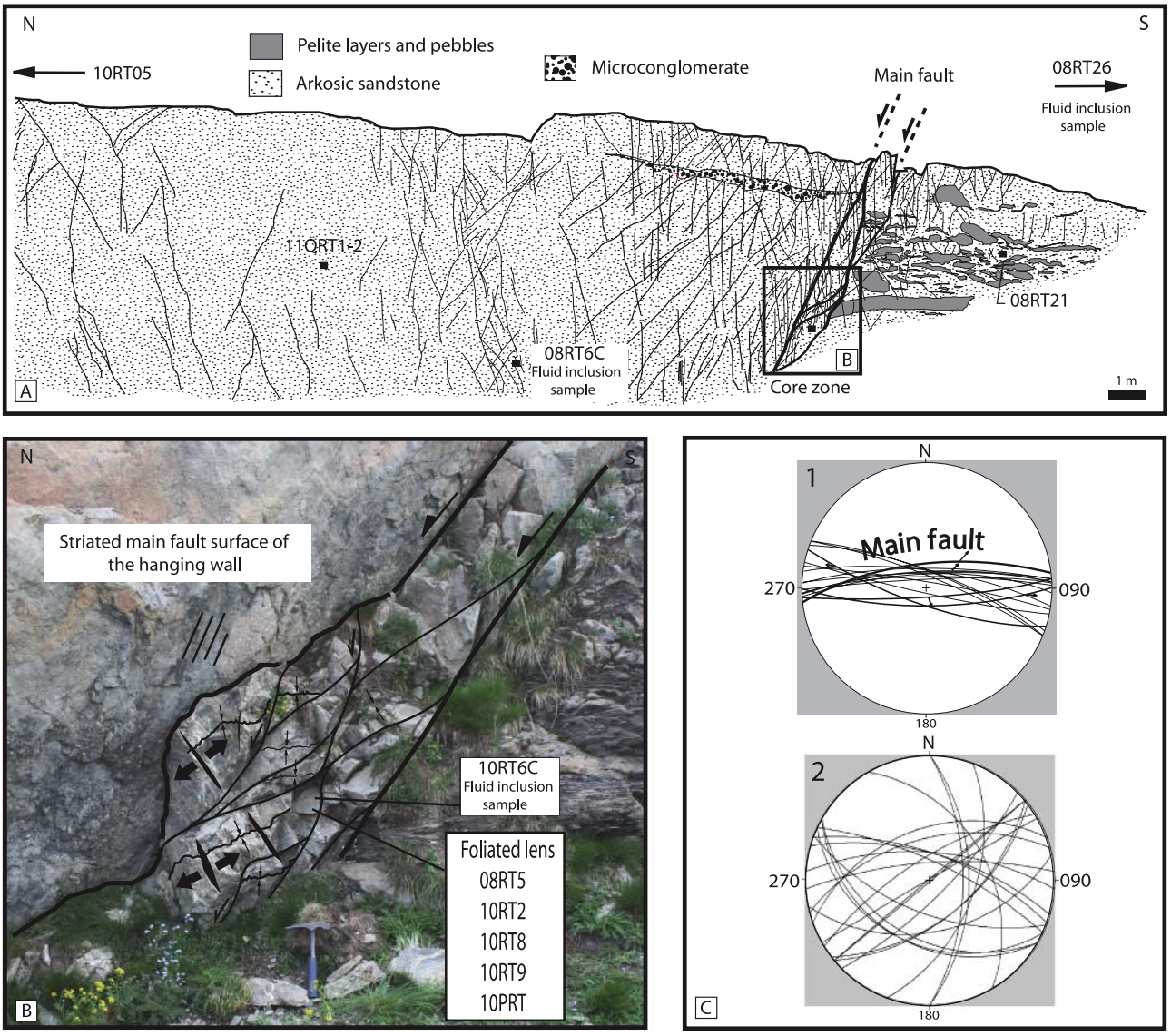

Figure 2. Restefond fault zone structure. (A) General view of the fault zone. (B) Detail of the fault core zone composed of imbricated foliated sandstone lenses and bounded by two major slip planes. The main offset is related with the northern plane. The rock hammer near the bottom of the photograph is for scale. (C) Structural data: slip planes and fractures of damage zone (arrows indicate the striation on slip planes) (1); veins in the foliated lenses of the core zone (2). The stereograms are lower-hemisphere equal-area stereographic projections.

The fault zone core, 1-m (3-ft) thick, is bounded by two slip surfaces and composed of tens of centimeters-size sandstone lenses featuring a more or less developed foliation (Figure 2A, B). The foliation visible in outcrop is composed of stylolites, phyllosilicate-rich layers, and an elongated shape fabric of grains in the coarse-grained components. The foliated sandstone lenses are bounded by north-dipping striated sliding planes with abundant phyllosilicate coating. Inside the lenses, the foliation strikes subparallel with the fault direction and shows a sigmoid geometry, defining an S-C structure typical of sheared rocks (Passchier and Trouw, 2005; Figure 2B). The S-C structure is composed of the newly formed foliation (S), which is cut by shear surfaces (C) that parallel the shear zone margins. Numerous extensional quartz or quartz-calcite veins as much as one centimeter wide and tens of centimeters long cut the foliation at a high angle, that is, coherent with the shortening direction deduced from the foliation. The density of stylolites and veins shows a positive correlation at the centimeter scale.

Except for sheared pelitic films bounding the foliated lenses, the pelite layers affected by the fault do not show strong shear deformation. They are cut by the slip surfaces and fractures without clay-smearing structures.

The northern main slip plane bears meter-long and tens of centimeters–wide steeply dipping grooves attesting normal main displacement. However, this plane and secondary planes in the fault zone also bear striations with variable dips, from normal to strike slip (Figure 2C1). The quartz-calcite vein directions are also variable, from parallel with normal to the fault trend (Figure 2C2). We interpret these variable slip and extension directions as traducing local movements caused by the complex geometry of the fault rock lenses. Late north–south calcite veins crosscut the fault zone and its hanging wall and footwall. We link them with the late north–south to north-northwest–south-southeast faults described by Kerckhove (1969) and Labaume et al. (1989) (Figure 1B).

The hanging-wall damage zone, approximately 6 m (20 ft) wide, features meter-long quartz-sealed fractures subparallel with the main slip plane and with steep (~70°) synthetic and antithetic dips (Figure 2C). The fracture density decreases with the distance from the main slip plane and transition to the background fracturing is gradual, with fracture spacing increasing from a few centimeters to tens of centimeters. The footwall damage zone is less well defined because of the limited development of fractures and heterogeneity of fracture distribution related to the chaotic internal structure of the slumped layer.

Point Vert Fault Zone Structure

The studied outcrop exposes two main normal faults—the Point Vert and Névé faults (the latter divided into two branches)—which dip southward approximately 70° and 60°, respectively (Figure 3). The normal displacement is 32 m (105 ft) for the Point Vert fault and 14 m (46 ft) for the Névé fault. Three normal faults with meter offsets occur between the two major faults.

The host succession is composed of (1) homolithic bodies composed of meter-thick sandstone beds and (2) heterolithic intervals with tens of centimeters–thick alternating sandstone and pelitic layers.

The Point Vert fault zone core consists of a 20-cm (8-in.)–thick band of gouge bounded by a few centimeters–thick band of sandstone featuring a foliation and quartz or quartz-calcite veins. The gouge is formed by a pelitic matrix containing up to centimeter-size lenses of foliated sandstone. Macroscopically, the foliated sandstone and associated veins are similar to those described above in the Restefond fault zone. The hanging-wall damage zone, 3 m (10 ft) wide, consists of anastomozing second-order normal faults with tens-of-centimeters spacing and offsets and east–west fractures with a quartz-calcite filling. The footwall is less visible and features poorly developed fracturing. The fault core zones of the Névé fault and secondary faults located between the major faults also feature lenses of foliated sandstone. Similar to the Restefond outcrop, the pelite layers affected by the faults show mainly brittle behavior and limited development of shear structures.

MICROSTRUCTURES

Host Sandstones Petrology

The host rocks of the Restefond and Point Vert outcrops are poorly sorted, fine to coarse-grained arkosic sandstones composed mainly of quartz, K-feldspar, plagioclase, phyllosilicate (biotite, white micas, and chlorite) grains, and lithic fragments (granite and metamorphic or volcanic rocks) (Figure 4A). Leclère et al. (2012) report approximately 30% to 40% of quartz, an equivalent proportion of feldspars, approximately 10% of phyllosilicates, and 15% of lithic fragments in the Restefond host rocks. Carbonate content is low, with dispersed detrital grains and a small amount of cement. The intense compaction and high grade of diagenesis are marked by the strong suturation of grain contacts caused by pressure solution (resulting in a shape fabric of grains with the long axis parallel with bedding); the absence of macroporosity (except the present meteoric dissolution of calcite cement); the

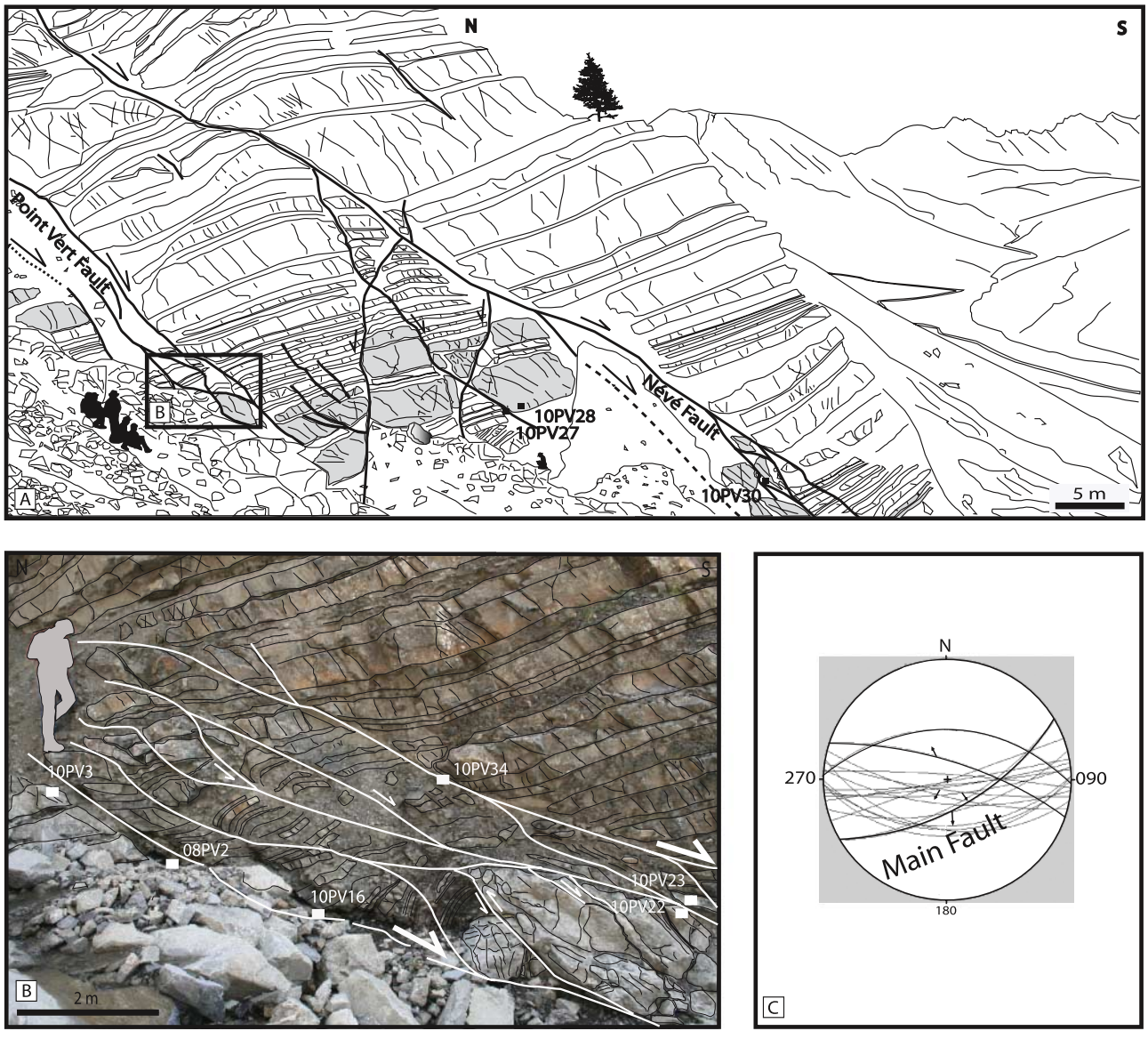

Figure 3. Point Vert fault zone structure. (A) General view of the Point Vert and Névé fault system. (B) View of the core zone and hanging-wall damage zone of the Point Vert fault. (C) Orientation of slip planes (arrows indicate striation). The stereograms are lower-hemisphere equal area stereographic projections. 10PV27 is the sample location.

partial sericitization of all types of feldspars, especially at grain boundaries; and the illitization of clay minerals (Labaume et al., 2009). Quartz overgrowths are absent, probably because of intense early compaction.

Fault Core Foliated Sandstone Microstructure

The microstructural characteristics of the foliated sandstones are similar in samples from both the Restefond and Point Vert outcrops. The foliation results from the combination of several types of deformation structures:

1. A shape fabric of the quartz and feldspar grains given by the combination of (1) stylolitization of the grain contacts parallel with the grain long axes and (2) closely spaced extensional microfractures normal to the stylolitized grain contacts (Figure 4B, C). Most of these fractures are intragranular (i.e., limited to a single grain) and have less than 0.1-mm opening displacements. They are sealed mainly by authigenic quartz-forming

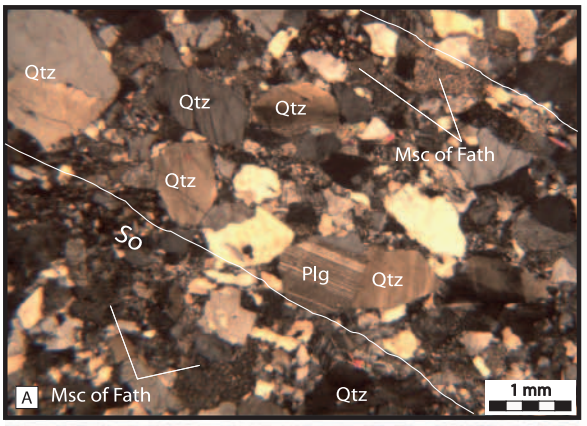
Qtz
Qtz
Qtz
Msc of Fath
Qtz
So
Plg
Qtz
A
Msc of Fath
Qtz
1 mm

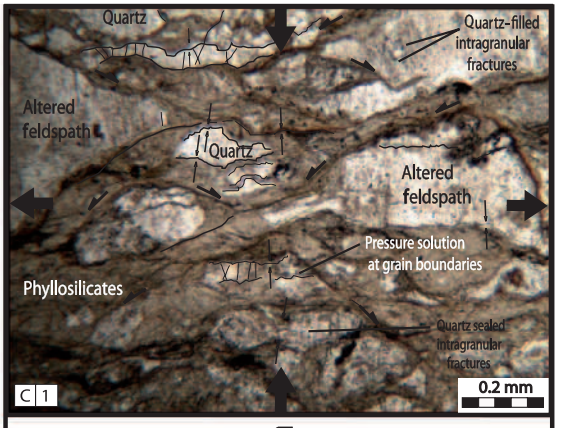
Quartz
Quartz-filled intragranular fractures
Altered feldspath
Quartz
Altered feldspath
Pressure solution at grain boundaries
Phyllosilicates
Quartz sealed intragranular fractures
C 1
0.2 mm

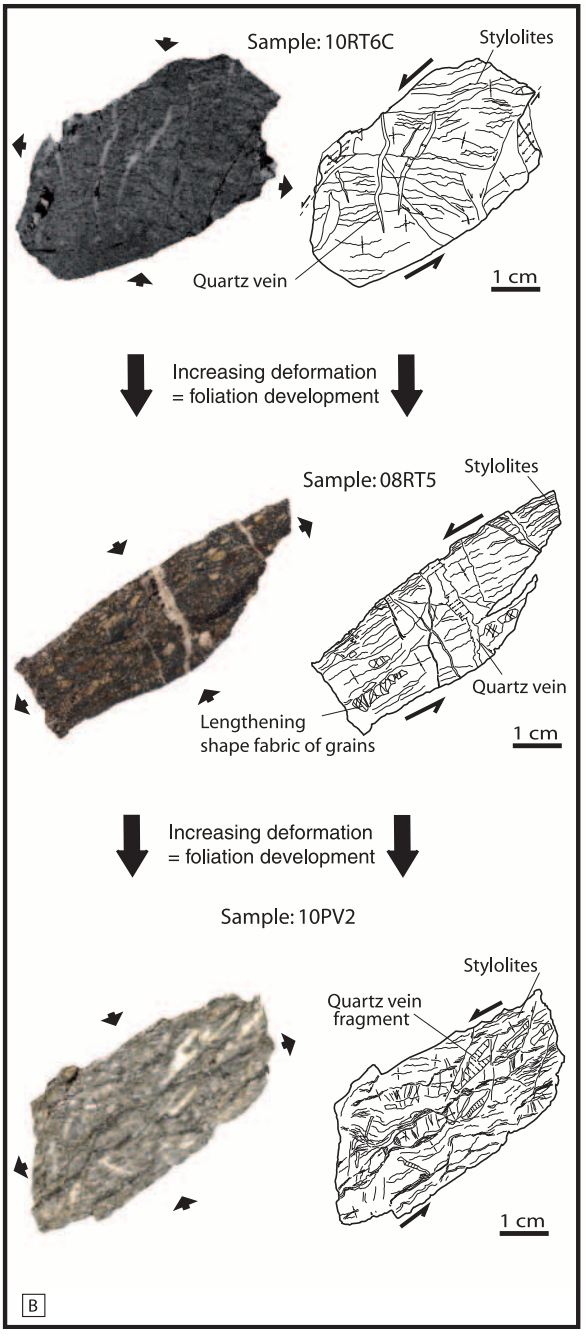
Sample: 10RT6C
Stylolites
Quartz vein
1 cm
Increasing deformation = foliation development
Sample: 08RT5
Stylolites
Quartz vein
Lengthening shape fabric of grains
1 cm
Increasing deformation = foliation development
Sample: 10PV2
Stylolites
Quartz vein fragment
1 cm
B

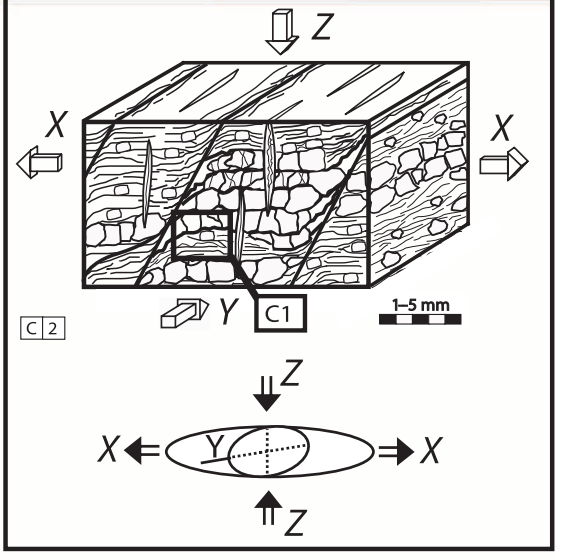
Z
X
X
Y
C1
1–5 mm
C 2
Z
X
Y
X
Z

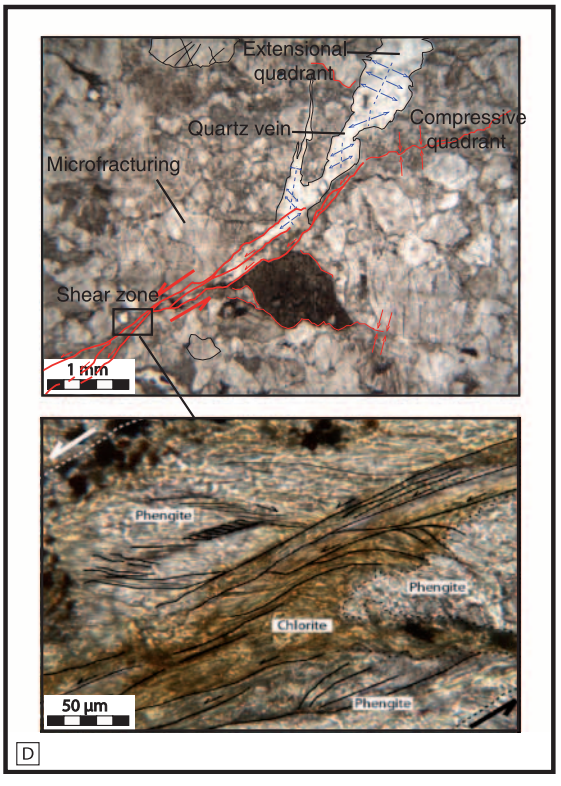
Extensional quadrant
Quartz vein
Compressive quadrant
Microfracturing
Shear zone
1 mm
Phengite
Phengite
Chlorite
Phengite
50 µm
D

overgrowths on the detrital quartz or, locally, by small (10–20 μm) newly formed white micas. The microfractures in the feldspar grains are filled by white micas and/or quartz; feldspar overgrowths are also locally present. Detrital mica grains generally lie parallel with the quartz and feldspar grain long axis.

2. Layers with a concentration of newly formed phyllosilicates associated with microfractured and disaggregated altered feldspar grains and intensely stylolitized and microfractured quartz grains. The newly formed phyllosilicates consist of white micas of phengitic composition (Leclère et al., 2012) and chlorite (Figure 4D). Microfractures are sealed by cements similar to those described above.

The foliation is cut by extensional microshear bands, with the direction of shear given by the curvature of the foliation fabric at shear band boundaries. The internal structure of shear zones is composed of (1) aligned detrital micas and newly formed, synkinematic white micas and chlorite (the latter generally concentrated along the shear zone core), (2) disaggregated altered feldspar grains, and (3) intensely fractured and quartz-sealed quartz grain fragments.

The association of microstructures defining the foliation and shear zones mimics at the millimeter scale the S-C structure observed at the outcrop scale and globally corresponds to a shortening normal to the foliation and an extension parallel with the foliation (Figure 4C).

As much as centimeter-wide transgranular extensional veins with quartz or quartz-calcite filling cut the foliation at a high angle, with orientations consistent with the directions of shortening and extension marked by the foliation (Figures 4B, D; 5). Some of them branch on shear zones in the extensional quadrant at shear zone extremities (Figure 4D). The vein cements feature two types of textures. A first type corresponds to elongate blocky quartz crystals with C axes at high angle to vein walls (referred to as fibrous veins in the following). Calcite crystals can be locally present between the quartz crystals. The vein fill features fluid inclusion planes subparallel with the vein walls, suggesting a progressive opening of the veins following a crack-seal mechanism (e.g., Becker et al., 2010). A second type corresponds to euhedral quartz crystals forming overgrowths over the detrital grains at vein walls and overlapped by later calcite crystals (Figure 6A, B). This type of crystallization corresponds to the geodic filling of open fractures. The fibrous veins can be as much as centimeters wide, whereas the geodic veins are systematically thinner. Crosscutting relationships show that the geodic veins are later than the fibrous veins. However, the geometric relationships show that both types of veins are related with the development of the foliation and shear zones.

Hence, the foliation, shear zone, and vein orientations allow definition of the orientation of the principal axes of the finite-strain ellipsoid (Ramsay, 1967), with the X (maximum principal strain) axis parallel with the foliation and normal to the veins, the Y (intermediate principal strain) axis parallel with the foliation and veins, and the Z (minimum principal strain) axis normal to the foliation and parallel with the veins (Figure 4C).

Visualization of Pore Structure

The pore space was observed in thin sections made from rock samples impregnated, first, under vacuum, and then, under pressure, with colored epoxy resin. The host rock pore network is mainly composed of (1) microporous films located along the grain contacts, (2) microporous areas associated with detrital or diagenetic phyllosilicate clusters in

Figure 4. Microstructures of the Point Vert and Restefond fault samples (Qtz = quartz; Msc = muscovitization; Plg = plagioclase; Fath = feldspar; So = stratification). (A) Microtexture of host rock (coarse-grained arkosic sandstone); note the light compaction-related shape fabric with long axis of grains parallel with bedding (10RT5 sample). (B) Different stages of foliation development at the sample scale. (C1 and C2) Microstructure of foliation (10PV2 sample) and associated finite strain ellipsoid; note the abundance of newly formed phyllosilicates compared to the host rock shown in panel A. (D) Microstructure of a shear zone composed of newly formed synkinematic white micas (phengite) and chlorite. Microstructure images were taken with an optical microscope under plain and polarized light (10RT6C sample).

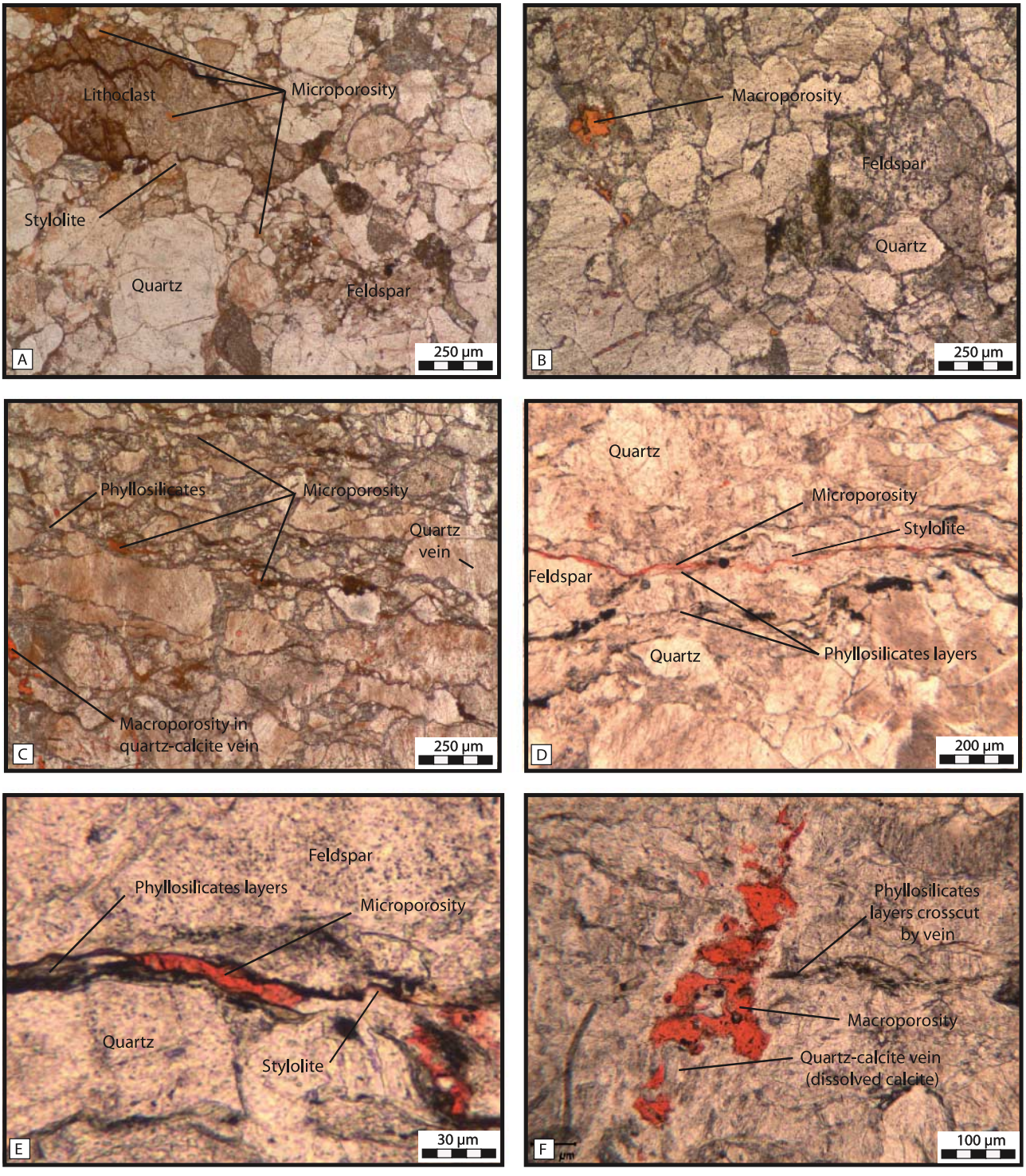

Figure 5. Aspects of porosity structure related to the different degrees and types of sandstone deformation. Porosity is revealed by the red color of impregnation epoxy resin. (A) Microporosity of host rock (coarse-grained arkosic sandstone) related to the stylolites, lithoclasts, and grain boundaries (10PV27 sample). (B) Macroporosity of host rock related to the calcite cement dissolution (weathering; 10RT5 sample). (C) Microporosity of foliated sandstone related to the detrital and newly formed phyllosilicates (10PV16A sample). (D) Macroporosity of quartz-calcite veins related to calcite dissolution (weathering) and crosscutting phyllosilicate layers (10RT2 sample). (E) Microporosity of foliated sandstone related to a mica layer within the foliation. (F) Macroporosity of foliated sandstone resulting from the dissolution of calcite cement in a quartz-calcite geodic vein. These pictures were taken with an optical microscope under plain light.

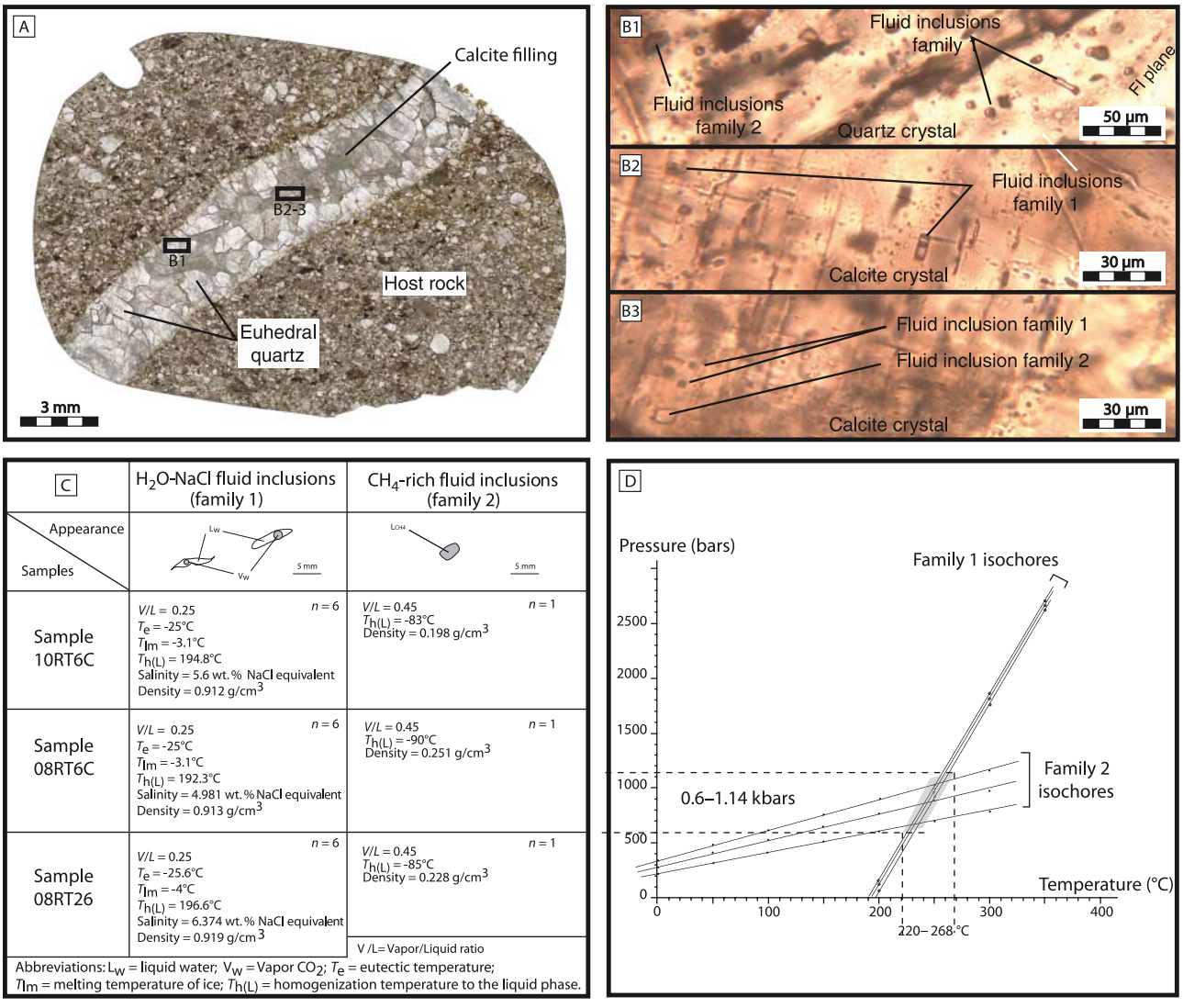

Figure 6. (A) Euhedral quartz-calcite sealed vein (sample 08RT26; scan image of thin section). The quartz crystals constitute a geodic filling overlapped by later calcite crystals. (B) Families 1 and 2 fluid inclusions (see comments in the text) plain light optical microscope picture. (C) Synthesis of microthermometric fluid inclusion data of the three studied vein samples from the Restefond fault zone. (D) Isochores and computation of the fluid trapping temperature (see comments in the text).

intergranular spaces, (3) intercrystalline microporosity in more or less sericitized feldpars (altered during late magmatic processes and/or burial diagenesis), and (4) intragranular microporosity in some lithic fragments (Figure 5A, B). Several macropores are also observed at triple-point grain contacts in the Point Vert samples. Macropores are relatively abundant in the Restefond samples because of the dissolution of carbonates (grain or cement) by outcrop weathering (Figure 5B), whereas they are poorly developed in the Point Vert samples.

In addition to the same pore structures as those observed in host rocks, the foliated sandstones show specific pore structures associated with structural heterogeneities. A first type corresponds to relatively continuous and sinuous microporous bands developed along stylolites and newly formed phyllosilicate clusters and made up of micropores located between subparallel phyllosilicate flakes (Figure 5C–E). A second type corresponds to microresidual (and a few macroresidual) pore spaces between crystal borders in the quartz-calcite veins. Finally, a third type corresponds to macropores in veins resulting from calcite dissolution by outcrop weathering, particularly developed at Restefond (Figure 5F).

PRESSURE AND TEMPERATURE CONDITIONS OF DEFORMATION

The mineralogical assemblages composed of synkinematic white micas and chlorite suggest that the studied faults were active at temperatures of at least 200°C (Mullis et al., 2002). This is confirmed in the case of the Restefond fault zone, where Leclère et al. (2012) found a temperature of 200°C ± 20°C for the precipitation of synkinematic chlorite using thermodynamic modeling of the chlorite chemical composition (Vidal et al., 2001). To better quantify the pressure and temperature (P-T) conditions of deformation, we performed a fluid inclusion study on the cements infilling the extensional veins.

Fluid Inclusions

Three samples from the Restefond fault core zone (08RT26, 08RT6C, and 10RT6C) were selected for fluid inclusion study (see location in Figure 2). They consist of quartz-calcite veins from the two types described in a preceding section, that is, fibrous veins in samples 08RT6C and 10RT6C and geodic veins in sample 08RT26 (Figure 6A). Identification and microthermometric study of fluid inclusions were made on double-polished, 100 µm–thick thin sections (Figure 6B). Typology and microthermometric data are summarized in Figure 6C.

Fluid Inclusion Petrography

Two families of fluid inclusions were identified in the three samples, in both quartz and calcite crystals from the two vein types (Figure 6B). Inclusions from both families occur isolated in the core of crystals and hence are interpreted as contemporaneous primary inclusions. The family 1 inclusions are the most abundant and correspond to two-phase inclusions at room temperature, with an average vapor-to-liquid ratio of 0.25. These inclusions are 2 to 10 µm in size and exhibit elongated, sometimes sigmoid, shapes. Family 2 comprises monophase inclusions filled by liquid at room temperature. These inclusions are rare, and have sizes ranging from 2 to 5 µm and a regular shape. Fluid inclusion planes are also present but, because of their very small size, these inclusions have not been investigated in this study.

Microthermometry (21 Fluid Inclusions in Three Samples)

The first melting temperature of family 1 inclusions, that is, the temperature at which liquids first coexist with solids (eutectic temperature), ranges from –28°C to –18°C with a mode at –25°C (Figure 6C). This average temperature agrees with published eutectic temperatures for the NaCl-H_20 system (–22.9°C, Crawford, 1981; –21.2°C, Borisenko, 1977). Ice melting temperature occurs between –4°C and 0°C (–11°C for H_2O-NaCl-CH_4 system; Becker et al., 2010). This implies very low salinities, ranging from 4.9 to 6.3 wt. % NaCl equivalent using the equations of Brown and Lamb (1989). Homogenization temperatures (in the liquid phase) are between 198°C and 227°C. Calculated densities, using the equations of Brown and Lamb (1989), are between 0.912 and 0.919 g/cm^3 (Figure 6C).

The family 2 inclusions become two-phase inclusions at temperatures lower than –120°C. During the heating stage, homogenization occurs between –90°C to –85°C, thus suggesting pure CH_4 inclusions (Goldstein and Reynolds, 1994; Becker et al., 2010). During the two-phase stage, the vapor-to-liquid ratio is close to 45% (Figure 6C). Densities bracketed between 0.198 and 0.251 g/cm^3 are determined using the FLINCOR fluid inclusion chemistry analysis program (Brown, 1989; Figure 6C).

Our petrographic observations give evidences for immiscibility in a water-salt-gas system, responsible for the simultaneous trapping of water-rich inclusions (family 1) and gas-rich ones (family 2). Because the two fluid inclusion families are contemporaneous and coeval to vein formation, microthermometry data can be used to determine the temperature, pressure, and fluid composition that prevailed during quartz and calcite crystallization within veins. Two methods can be used. First, we can use the intersecting isochores of these two fluid inclusion families as commonly realized within classic fluid inclusion studies (e.g., Chauvet et al., 2001). The second method is suggested by Goldstein and Reynolds (1994). They propose that, in the

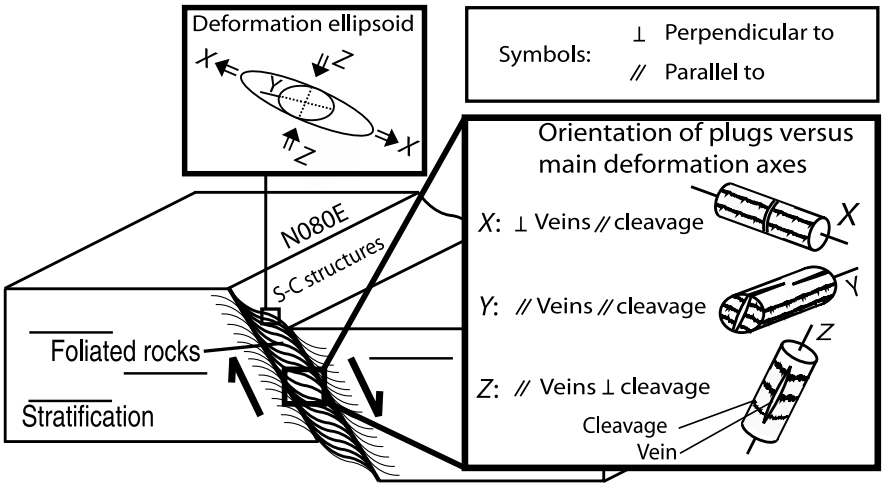

Figure 7. Orientation of petrophysical plugs following the principal strain axes (see comments in the text). The S-C structure is composed of the newly formed foliation (S), which is cut by shear surfaces (C) that parallel the shear zone margins.

case of entrapment of a single phase of an immiscible fluid system, the homogenization temperature (T_h) yields the true temperature of trapping (T_t). The T_h of the aqueous system is used because CH_4-rich inclusions may contain invisible H_2O (i.e., they may not be single-phase ones). Extending the methane isochore herein calculated with the FLINCOR program until the T_t allows defining the pressure of entrapment. A third method (Becker et al., 2010), which allows determining the temperature and pressure of fluid entrapment with a single isochore, cannot be used here in the absence of direct analysis of fluid composition.

Results from the two methods are shown in Figure 6D. Isochores were constructed for the two fluid inclusion families using the FLINCOR computer program (Brown, 1989) to average the microthermometric values indicated in Figure 6C. The temperature of the vein formation of 220°C to 268°C at a pressure of 0.6 to 1.14 kbars is obtained with the first method, whereas the second method gives a lower temperature (195°C–200°C) at similar pressure.

PETROPHYSICAL CHARACTERISTICS

Sample Selection

Deformation in the studied fault zone cores is characterized by a (semi)penetrative foliation of sandstone lenses. To characterize the matrix petrophysical properties of these particular fault rocks, samples were chosen as representative of various degrees of deformation intensity, and reference host sandstones were sampled outside fault zones (see sample location in Figures 2, 3). To better compare the results from the different samples, only medium to coarse-grained sandstones were tested. The pelite layers, which show mainly brittle behavior, were not tested. The fault gouge, present only in one of the fault zones on the Point Vert outcrop, is a late feature not representative of the P-T conditions of fault zone deformation described in this article and was not tested.

Plug Orientation

For studying fault zone petrophysical properties, most authors use fault strike or bedding plane to choose test plug orientations (Faulkner and Rutter, 1998; Surma et al., 2003; Richard and Sizun, 2011; Leclère et al., 2012). In this study, we aimed to investigate the anisotropy of the matrix petrophysical properties of the foliated fault rocks and thus chose the drilling directions of the plugs considering the sample microstructure.

Petrophysical measurements were performed on cylindrical plugs of 2-cm (0.8-in.) diameter and 2- to 5-cm (0.8–2.0-in.) length, drilled in oriented blocks sampled at the outcrop. On each block, as far as possible, three plugs were drilled in three perpendicular directions based on naked-eye visible microstructures. In the host sandstones, the three

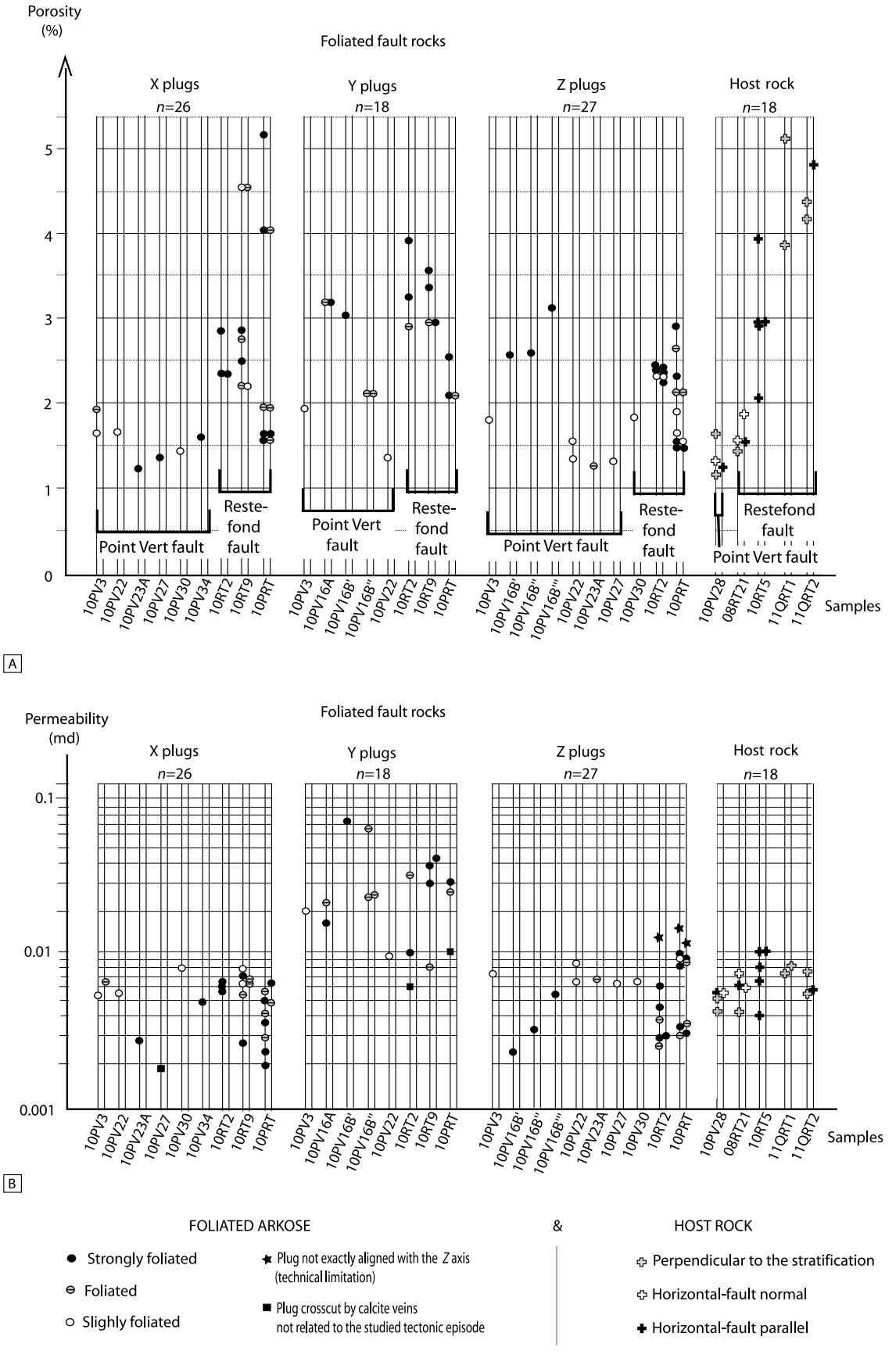

Figure 8. (A) Porosity data of Point Vert and Restefond fault rocks and host rocks samples (see comments in the text). (B) Permeability data of Point Vert and Restefond fault rocks and host rocks samples (see comments in the text).

plug orientations are (1) parallel with the bedding plane and to the fault strike, (2) parallel with the bedding plane and perpendicular to the fault strike, and (3) perpendicular to the bedding plane. In the case of deformed (foliated) sandstones, the three plugs are parallel with the principal axes of the finite-strain ellipsoid determined from the microstructural study, that is (Figure 7),

- the X axis, parallel with the foliation and normal to the extension veins (X axis plugs),
- the Y axis, parallel with the foliation and to the extension veins (Y axis plugs), and
- the Z axis, normal to the foliation and parallel with the extension veins (Z axis plugs).

We sampled plugs in sandstones with different degrees of deformation, that is, slightly foliated, foliated, and strongly foliated, to investigate the effect of fabric development on the petrophysical properties of fault rocks. Plugs were selected to have the best homogeneity of microstructures but, in some cases, macrostructures such as veins crosscut the studied plugs, and their influence is discussed further.

To our knowledge, this petrophysical approach is new and relevant for determining the matrix permeability of fault rocks because the measurement orientation is always consistent with the orientation of structural heterogeneities.

Measurement Methodology

Plug total porosity was measured using the Archimedes method, and gas permeability measurements were made using the steady-state flow method. Methodological details are given in the Appendix.

Porosity Results (89 Plugs in 32 Samples)

Most of the total porosity values range from 1% to 3% for both the Point Vert and Restefond faults (Figure 8A). No significant difference exists between the host rock and foliated fault rock X, Y, and Z axes plug porosities. These values are consistent with those obtained by Labaume et al. (2009) in sandstones sampled outside fault zones in the same area. Values higher than 3% are found only in a limited number of plugs (16 plugs). Microstructural observation (Figure 5) suggests that these higher porosity values are caused by calcite cement dissolution (vein cement for plugs from fault zones and matrix cement in the case of the host rocks). This alteration is related to the present outcrop weathering and is more developed in the case of the Restefond outcrop, resulting in a mean value of porosity higher in the samples from this outcrop. However, these particular values are presented here because they can be used when discussing the porosity-permeability relationships (see below).

Permeability Results

Host Rocks (18 Plugs in 5 Samples)

The permeability values of the host rock plugs range from 0.0038 to 0.010 md, without significant differences between the two fault zones (Figure 8B). The values are equivalent in the three plug directions.

Foliated Fault Rocks: X Axis Plugs (26 Plugs in 9 Samples)

The permeability values of the X axis plugs range from 0.0019 to 0.0081 md (Figure 8B), that is, in the same order of magnitude (10^{-3} md) as the host rock values but with a wider range. The samples with moderately to strongly developed foliation yield values dispersed over this range, this dispersion probably reflecting the millimeter-scale structural heterogeneity. However, the fact that the values from samples with slightly developed foliation all range among the highest values, similar to those of the host rocks, suggests a tendency for a slight reduction of permeability parallel with the X axis with an increasing development of foliation.

Foliated Fault Rocks: Y Axis Plugs (18 Plugs in 8 Samples)

The permeability values of the Y axis plugs range from 0.006 to 0.07 md (Figure 8B). The representative order of permeability measured is 10^{-2} md, that is, one order of magnitude higher than the host rock, X axis, and Z axis values. The permeability is not clearly correlated with the degree of foliation development, with a dispersion probably reflecting the millimeter-scale structural heterogeneity. In at least two cases (10RT2 and 10PRT

samples), the lowest values are linked with cross-cutting veins not correlated with the Y axis theoretical framework. The other low values cannot be related to detectable technical or geologic anomalies.

Foliated Fault Rocks: Z Axis Plugs (27 Plugs in 10 Samples)

The permeability values of the Z axis plugs range from 0.0022 to 0.0114 md. Similarly to the X axis plugs, the data are grouped in the 10^{-3} md order of magnitude, comparable to that of the host rocks. The highest value of 10RT2 and the two highest values of 10PRT samples are explained by an angle (~45°) between the Z-strain axis and the plug axis, these plugs being thus intermediate between the theoretical Y and Z axes. For the other plugs, the distribution of values according to the intensity of the foliation is similar to that observed for the X axis samples, also suggesting a tendency to a slight permeability reduction parallel with the Z axis with increasing intensity of foliation.

Permeability Versus Porosity

The results presented above and illustrated in Figure 8 show the absence of clear correlation between porosity and permeability when comparing the different groups of samples. In the host rock case, the Restefond plugs have a higher porosity (related to the calcite cement dissolution by weathering) than the Point Vert plugs for a similar range of permeability. In the case of the foliated fault rocks, the Y axis plugs, which yield the higher permeability values, have a range of porosity values similar to those of the X and Z axes plugs and host rocks. Figure 9 illustrates with more detail the relative independence between porosity and permeability values at the scale of the individual samples of decimeter size where plugs in the three directions are available. For instance, in the 10PV3 sample, the increase of permeability for the Y axis plug is correlated with a small increase of porosity compared to the X and Z axes plugs, whereas the 10PV22 sample shows a Y axis plug having the lowest value of porosity for the highest permeability compared to the X and Z axes plugs of the same sample.

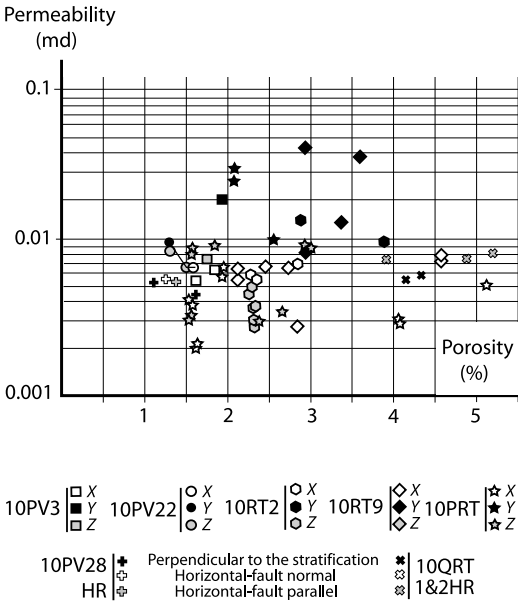

Figure 9. Relationship between permeability and porosity in Point Vert and Restefond fault rocks and host rocks samples (see comments in the text).

DISCUSSION

Our fluid inclusion study shows that the Restefond fault was active in a temperature range of 195°C to 268°C and a pressure range of 0.6 to 1.14 kbars. These temperatures match the thermodynamical modeling of synkinematic chlorite chemistry in the Restefond fault zone (Leclère et al., 2012). These P-T conditions of fault activity are close to those of the maximum burial depth (8–10 km [5–6 mi]) of the Grès d'Annot in the study area, deduced from vitrinite reflectance data assuming a geothermal gradient of 25°C to 30°C/km (Labaume et al., 2009). They argue for vein formation at fluid pressures intermediary between hydrostatic and lithostatic pressures. The deep setting of fault activity suggests that the studied normal faulting may have resulted from gravitational collapse related to the first stage of basement uplift, before significant erosion of the overlying Embrunais-Ubaye nappes. The deformation related to the synsedimentary activity of the Point Vert and Névé faults described by Bouroullec et al. (2004) has probably been masked by the later activity described in this study.

The arkosic petrology and deep burial context favored the close association of fracturing with

fluid-rock interactions, which controlled the two main structural heterogeneities characterizing the fault rocks, that is, foliation and veins. In particular, the high feldspar content of the protolith favored the precipitation of the synkinematic phyllosilicates forming the foliation, with white micas resulting from a process of muscovitization of feldspars in the presence of fluids (Leclère et al., 2012). This reaction also releases silica, which is likely to have participated in quartz precipitation in veins, together with the silica directly derived from the pressure solution of detrital quartz grains. A similar process of feldspar muscovitization has been already described in quartz-feldspathic crystalline fault rocks (Wibberley, 1999), but, to our knowledge, the fault zones described here are the first ones where this process is described in sedimentary rocks and where permeability measurements are performed on this type of fault rocks (Leclère et al., 2012). The significant number of petrophysical measurements oriented following the principal axes of deformation (89 pairs of porosity and permeability values) shows that the foliation and veins, which we correlate with orientation and magnitude of the finite-strain ellipsoid, control the matrix permeability of the fault zone core.

Relations between Microstructures and Plug Permeability

Equivalent permeability values in the host rocks from the Restefond and Point Vert outcrops demonstrate that the macroporosity of the Restefond samples (caused by the presence of local calcite dissolution by weathering [Figure 5B]), does not influence permeability. The microporosity seems to be the first-order parameter controlling the plug permeability in the host rock of the two faults.

In the foliated fault rocks, microscopic observation suggests that the preferential flow path is mainly located within the microporosity along the surfaces parallel with the (001) plane of phyllosilicates forming the foliation (Figure 5). These surfaces correspond to a tectonic cleavage that coincides with the flattening plane (X,Y) of the finite-strain ellipsoid. However, the permeability measurements along the X axis yield values in the same order of magnitude (10^{-3} md) as the host sandstone, with a tendency to a slight reduction with increasing intensity of foliation. These results suggest that the cements of the veins, which crosscut the X axis (Figure 5F), interrupt the continuity of the 001 phyllosilicate planes and have a restrictive effect on plug permeability following the X axis, which remains equivalent to, or slightly lower than, that of the host rock. By contrast, the Y axis is parallel with both the (001) plane of phyllosilicates and the veins. Fluid flow along the foliation plane is not restricted by transverse veins in this direction, resulting in the higher plug permeability values (10^{-2}-md order of magnitude) than along the X axis.

In the case of the Z axis plugs, permeability values in the same order of magnitude as the host sandstone, with a tendency to a slight reduction with increasing intensity of foliation, illustrates the restraining effect of foliation for fluid flow perpendicular to the (001) plane of phyllosilicates.

The function of veins on plug permeability can be discussed further in the case of the Z axis, parallel with veins and normal to cleavage. In that case, the Restefond (where vein calcite cements are dissolved by weathering alteration) and Point Vert (where vein calcite cements are not dissolved) samples have the same order of magnitude of permeability (10^{-3} md), similar to the host rock values. These data suggest that the veins are not connected and, even if vein permeability may be enhanced by dissolution, the effective permeability at a scale larger than the vein length (here the centimeter-scale of plugs) remains controlled by the permeability of the foliated matrix separating the veins (Philip et al., 2005; Olson et al., 2009).

Permeability Ellipsoid and Normal Fault Zone Permeability Model

This work shows the link between the finite-strain ellipsoid of foliated fault rocks and the anisotropy of their matrix permeability, which can be expressed as a permeability ellipsoid (Figure 10A). This ellipsoid is a prolate ellipsoid of revolution, with a major permeability axis parallel with the Y axis of the finite-strain ellipsoid and a lower and constant value of permeability in the orthogonal

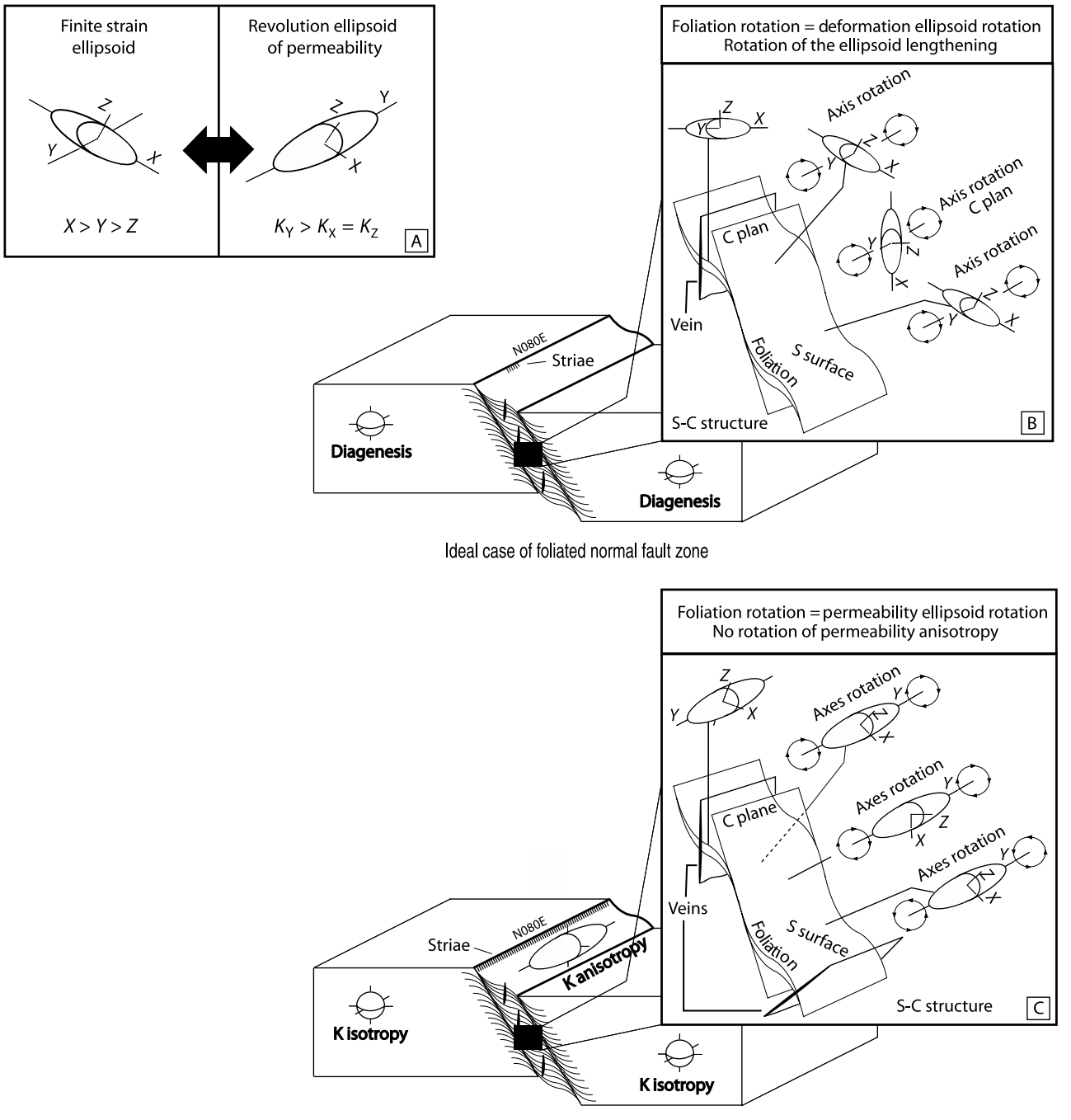

Figure 10. Relationships between structural organization and permeability (*K*) anisotropy in a theoretical case of normal fault zone affecting a feldspar-rich protolith in deep diagenesis conditions. (A) Relation between finite-strain ellipsoid and ellipsoid of permeability. (B) Finite-strain ellipsoid rotation related to S-C structures composed of the newly formed foliation (S), which is cut by shear surfaces (C) that parallel the shear zone margins. (C) Rotation of the related revolution ellipsoid of permeability (see comments in the text).

directions. Permeability values show that the anisotropy of permeability increases with the ratio of maximum to minimum principal strains (X to Z axes of the finite-strain ellipsoid).

To upscale the implication of our results obtained at the plug scale, we must consider the effects of the development of S-C structures at various scales across the fault zone (Figures 2B; 4B,

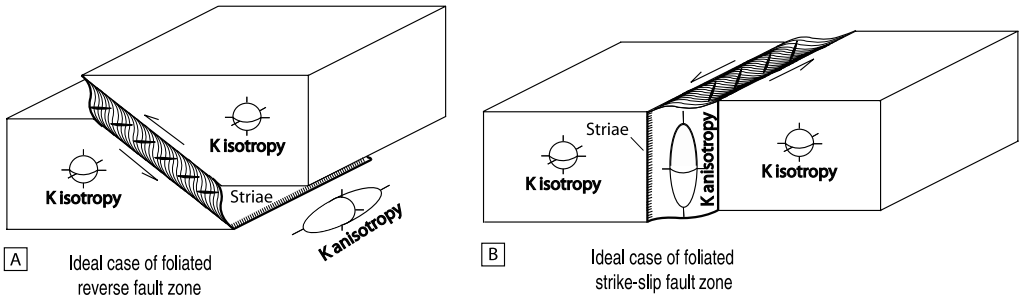

Figure 11. Extrapolation of results from this study: inferred permeability (*K*) anisotropy of theoretical reverse (A) and strike-slip (B) fault zones affecting a feldspar-rich protolith in deep diagenesis conditions.

C). Figure 10B illustrates in a simple theoretical case of normal fault zone how the foliation and veins rotate in relation to the sigmoid geometry of S-C structures. This corresponds to a rotation of the finite-strain ellipsoid around the Y axis, which, in the case of a normal fault zone, is typically horizontal and parallel with the fault trend. Because of this rotation, the X axis orientation can range from horizontal to parallel with the striation on the slip (C) surfaces, whereas the Z axis orientation ranges from subvertical to normal to the slip surfaces. Hence, the rotation of the finite-strain ellipsoid around the Y axis does not influence the anisotropy of permeability because the highest value remains horizontal and parallel with the fault azimuth (Figure 10C).

Generalization of Results

At equivalent petrological and P-T conditions to those studied here (i.e., quartz-feldspathic composition and high temperature favoring the development of foliation and veins in fault rocks), results similar to those obtained here on normal faults may be expected in the other fault zone types. In the case of a reverse foliated fault zone, the intermediate (Y) principal strain axis is subhorizontal and parallel with the fault, similar to the normal fault case, whereas it is subvertical in the case of a strike-slip fault. More generally, the Y strain axis is parallel with the fault plane and normal to the striation on the fault surface. Hence, this direction may correspond to that of the highest permeability in foliated fault rocks in the different fault zone types (Figure 11).

Comparison with Previous Studies

The fact that shearing deformation may induce a higher effective permeability in the direction perpendicular to the shear displacement has already been observed in both the analogical and numerical modeling of shear zones in low-porosity sandstones where fluid flow channeling is related to the roughness of the slip surface (e.g., Koyama et al., 2004; Auradou et al., 2006). Although the aperture typology obtained in these experiments is different from the foliation described here, the anisotropy of permeability related to fault fabric has a similar orientation.

At the fault zone scale, the classical model of Caine et al. (1996) suggests that the damage zone is a zone of fluid conduits in fractures, whereas the core zone is a barrier caused by rock grain-size reduction and/or mineral precipitation. However, in deeply buried sandstones, the activation of pressure solution and cementation of quartz at temperatures higher than 80°C (Renard and Ortoleva, 1997; Lander et al., 2008; Becker et al., 2010) tends to seal the fractures that then become ineffective conduits for fluid flow (Laubach, 2003). Structural and petrophysical studies in various examples of deeply buried quartz-rich sandstones confirm the reduction of permeability in the core zone caused by grain-size reduction and/or quartz cementation (Fisher et al., 2003; Surma et al., 2003; Balsamo et al., 2010). Hence, both the fault core and damage zones are likely to act as barriers to fluid flow in deeply buried sandstones. Our case study conforms to this inference in the case of the damage zones where fractures may have acted as fluid conduits during deformation but are now sealed by quartz or quartz-calcite cements. By contrast, we show that a potential postdeformation fluid drain occurs in the core zone along the Y principal deformation axis of the foliated lenses. Moreover, these foliated fault zones show a permeability anisotropy that is not described in quartz-rich fault zones. These

comparisons highlight the importance of the arkosic lithology (i.e., the high feldspar content of the host rock) in the precipitation of synkinematic phyllosilicates and their potential impact on the hydraulic properties of fault zones in deeply buried reservoirs.

CONCLUSIONS

A combined structural and permeability analysis has been conducted on two normal faults formed in low-porosity arkosic sandstones under deep diagenesis conditions (temperature range of 195°C–268°C and pressure range of 0.6–1.14 kbars, according to fluid inclusion microthermometry). Deformation mechanisms in the fault zone cores are characterized by the close interaction of intense fracturing, pressure solution, quartz cementation, and synkinematic phyllosilicate neoformation caused by feldspar alteration. Foliation and veins are the two main structures resulting from these mechanisms and provide bases for estimating the orientation of the finite-strain ellipsoid.

Petrophysical plug drilling parallel with the principal (X, Y, and Z) axes of the finite-strain ellipsoid of foliated fault rocks was performed to characterize the influence of fault zone deformation on the permeability anisotropy:

1. The Y direction, here defined as parallel with the intermediate (Y) principal strain axis (parallel with the intersection between foliation and veins), has the highest permeability values (10^{-2} md), resulting from fluid circulation along microporosity associated with the 001 plane of the phyllosilicate flakes forming the foliation. The X direction, parallel with the maximum (X) principal strain axis (parallel with foliation and perpendicular to veins), Z direction, parallel with the minimum (Z) principal strain axis (perpendicular to foliation), and host rocks have similar values of permeability, one order of magnitude lower than that along the Y axis (10^{-3} md).
2. The tendency to a slight reduction of permeability along the X and Z axes with increasing intensity of foliation enhances the anisotropy of permeability resulting from foliation development.

The resulting permeability ellipsoid at the centimeter scale is a revolution ellipsoid with a long axis parallel with the Y axis and that is not affected by the changes of foliation dip in the S-C structures defining the structural fabric of the fault zone core. We suggest that these conclusions made on foliated normal fault zones may apply to other fault types (reverse or strike-slip) formed in similar petrological and P-T conditions (i.e., arkosic composition and high temperature favoring the development of foliation and veins). Hence, the generalization of our results would be that the highest permeability direction in foliated fault rocks likely to exist in deeply buried reservoirs is parallel with the fault and perpendicular to the slip direction on the fault plane.

These results contrast with previous studies in quartz-rich fault zones formed in deep settings, where the fault cores are barriers to fluid flow because of grain-size reduction and quartz cementation. They highlight the importance of the high feldspar content of the host rock in the precipitation of synkinematic phyllosilicates and their potential impact on the hydraulic properties of fault zones in deeply buried reservoirs. However, further studies are needed to explore this effect in variable conditions, in particular, its relation with fault throw and its dependence to the fluid pressure and fault kinematics.

APPENDIX: MEASUREMENT METHODOLOGY

Porosity Measurement Procedure

Total porosity (connected porosity) was measured using the Archimedes method (Monicard, 1975; Zinsner and Pellerin, 2007) to characterize porosity-permeability relationships. Plugs are first dried in an oven at 60°C until they reach a stable mass (m_d) and then put upright in an airtight enclosure for 24 hr at room temperature under vacuum at 2.6 Pa. They are progressively imbibed from their base with degassed distilled water, under a dynamic vacuum. The total porosity Φ (%) is given by: $\Phi = [(m_1 - m_d) / (m_1 - m_2)] \times 100$, where m_1 is the mass of the sample saturated with water and m_2 is the mass of the sample saturated with water weighed under water (hydrostatic underwater weighing).

Absolute Permeability Testing Procedure

Gas permeability measurements were made using the steady-state flow method that consists of imposing a known pore-pressure difference across the specimen and measuring the resultant flow rate that is proportional to permeability. The cylindrical plug is placed in a rubber sleeve in a Hassler cell (Mertz, 1991). The gas used for the test is nitrogen. A confining pressure (20 bars) is applied on the sleeve to bond it tightly against the specimen to prevent any gas flow between the plug and the sleeve. Confining pressure and pore-fluid pressures on both sides of the specimen were controlled using high-precision manometers. The flow rate out of the sample is measured using a flow tube meter. Absolute permeability (K) is determined by application of Darcy's law expressed as

$$Q = \frac{K}{\eta} S \frac{\Delta P}{L}$$

where Q is the gas flow rate out of the sample, K is the absolute permeability, S is the cross-sectional area of the plug, ΔP is the gas pore-pressure difference accross the sample, η is the dynamic viscosity of the gas, and L is the length of the sample. The laminar character of the gas flow is verified by determining the Reynolds number. About ten permeability measurements at various pore-pressure gradients were conducted for each sample to correct for the Klinkenberg effect using the graphical method described by many authors (Riepe et al., 1983; Rushing et al., 2004; Zinsner and Pellerin, 2007).

REFERENCES CITED

Antonellini, M. A., and A. Aydin,1994, Effect of faulting on fluid flow in porous sandstones: Petrophysical properties: AAPG Bulletin, v. 78, p. 355–377.

Auradou, H., G. Drazer, A. Boschan, J-P. Hulin, and J. Koplik, 2006, Flow channeling in a single fracture induced by shear displacement: Geothermics, v. 35, p. 576–588, doi:10.1016/j.geothermics.2006.11.004.

Aydin, A.,1978, Small faults formed as deformation bands in sandstones: Pure and Applied Geophysics, v. 116, p. 913–930, doi:10.1007/BF00876546.

Balsamo, F., F. Storti, F. Salvini, A. Silva, and C. Lima, 2010, Structural and petrophysical evolution of extensional fault zones in low-porosity, poorly lithified sandstones of the Barreiras Formation, NE Brazil: Journal of Structural Geology, v. 32, p. 1806–1826, doi:10.1016/j.jsg.2009.10.010.

Becker, S. P., P. Eichhubl, S. E. Laubach, R. M. Reed, R. H. Lander, and R. J. Bodnar, 2010, A 48-m.y. history of fracture opening, temperature, and fluid pressure: Cretaceous Travis Peak Formation, east Texas Basin: Geological Society of America Bulletin, v. 122, p. 1081–1093, doi:10.1130/B30067.1.

Bigot-Cormier, F., M. Sosson, G. Poupeau, J. Stephan, and E. Labrin, 2006, The denudation history of the Argentera Alpine external crystalline massif (western Alps, France-Italy): An overview from the analysis of fission tracks in apatites and zircons: Geodinamica Acta, v. 19, no. 6, p. 455–473, doi:10.3166/ga.19.455-473.

Borisenko, A. S., 1977, Study of the salt composition of gas-liquid inclusions in mineral by the cryometric method: Soviet Geology and Geophysics, v. 18, p. 11–19.

Bouroullec, R., J. A. Cartwright, H. D. Johnson, C. Lansigu, J. Quemener, and D. Savanier, 2004, Syndepositional faulting in the Grès d'Annot Formation, SE France: High-resolution kinematic analysis and stratigraphic response to growth faulting: Geological Society (London) Special Publication 221, p. 241–265.

Brown, P. E., 1989, FLINCOR: A microcomputer program for the reduction and investigation of fluid inclusion data: American Mineralogist, v. 74, p. 1390–1393.

Brown, P. E., and W. M. Lamb, 1989, P-V-T properties of fluids in the system $H_2O^{+/-}$ $CO_2^{+/-}$ NaCl: New graphical presentations and implications for fluid inclusion studies: Geochimica et Cosmochimica Acta, v. 53, no. 6, p. 1209–1221, doi:10.1016/0016-7037(89)90057-4.

Caine, J. S., J. P. Evans, and C. B. Forster, 1996, Fault zone architecture and permeability structure: Geology, v. 24, p. 1025–1028, doi:10.1130/0091-7613(1996)024<1025:FZAAPS>2.3.CO;2.

Cavailhes, T., R. Soliva, A. Benedicto, D. Loggia, R. A. Schultz, and C. A. J. Wibberley, 2009, Are cataclastic shear bands fluid barriers or capillarity conduits? Insight from the analysis of redox fronts in porous sandstones from Provence, France: European Association of Geoscientists and Engineers 2nd International Conference on Fault and Top Seals, Montpellier, France, September 21–24, 2009, 3 p.

Chauvet, A., P. Piantone, L. Barbanson, P. Nehlig, and I. Pedroletti, 2001, Gold deposit formation during collapse tectonics: Structural, mineralogical, geochronological and fluid inclusion constraints in the Ouro Preto Gold mines, Quadrilatero Ferrifero, Brazil: Economic Geology, v. 96, p. 25–48.

Corrigan, G., 1993, Estimation of recoverable reserves: The geologist's job: Petroleum Geology Conference Series, v. 4, p. 1473–1481.

Corsini, M., G. Ruffet, and R. Caby, 2004, Alpine and late Hercynian geochronological constraints in the Argentera massif (western Alps): Eclogae Geologicae Helvetiae, v. 97, p. 3–15, doi:10.1007/s00015-004-1107-8.

Crawford, M. L., 1981, Phase equilibria in aqueous fluid inclusions: Petrological Mineralogical Association of Canada Short Course in Fluid Inclusion, v. 6, p. 75–100.

Du Bernard-Rochy, X., 2002, Les modes de localisation et de propagation de la rupture dans les zones de failles affectant les grès, et les facteurs qui les contrôlent: Ph.D. thesis, Université Joseph Fourier, Grenoble, France, 305 p.

Eichhubl, P., W. L. Taylor, D. D. Pollard, and A. Aydin, 2004, Paleofluid flow and deformation in the Aztec sandstone, at the Valley of Fire, Nevada: Evidence for the coupling of hydrogeological, diagenetic and tectonic processes: Geological Society of American Bulletin, v. 116, p. 1120–1136, doi:10.1130/B25446.1.

Faulkner, D. R., and E. H. Rutter, 1998, The gas permeability of clay-bearing fault gouge at 20°C: Geological Society (London) Special Publication 147, p. 147–156.

Fisher, Q. J., and R. J. Knipe, 2001, The permeability of faults within siliciclastic petroleum reservoirs of the North Sea and Norwegian continental shelf: Marine and Petroleum Geology, v. 18, p. 1063–1081, doi:10.1016/S0264-8172(01)00042-3.

Fisher, Q., J. M. Casey, S. D. Harris, and R. J. Knipe, 2003, Fluid flow properties of faults in sandstone: The importance of temperature history: Geology, v. 31, p. 965–968, doi:10.1130/G19823.1.

Fossen, H., and A. Bale, 2007, Deformation bands and their influence on fluid flow: AAPG Bulletin, v. 91, no. 12, p. 1685–1700, doi:10.1306/07300706146.

Fossen, H., R. A. Shultz, Z. K. Shipton, and K. Mair, 2007, Deformation bands in sandstone: A review: Journal of the Geological Society of London, v. 164, p. 755–769, doi:10.1144/0016-76492006-036.

Fry, N., 1989, Southwestward thrusting and tectonics of the western Alps: Geological Society (London) Special Publication 45, p. 83–109.

Goldstein, R. H., and T. J. Reynolds, 1994, Systematics of fluid inclusions in diagenetic minerals: Society for Sedimentary Geology, Society of Economic Paleontologists and Mineralogists Short Course 31, 199 p.

Joseph, P., and S. A. Lomas, 2004, Deep-water sedimentation in the Alpine foreland basin of SE France: New perspectives on the Grès d'Annot and related systems—An introduction: Geological Society (London) Special Publication 221, p. 1–16.

Kerckhove, C., 1969, La zone du flysch dans les nappes de l'Embrunais-Ubaye (Alpes occidentales): Géologie Alpine, v. 45, p. 1–202.

Koyama, T., N. Fardin, and L. Jing, 2004, Shear-induced anisotropy and heterogeneity of fluid flow in a single rock fracture with translational and rotary shear displacements: A numerical study: International Journal of Rock Mechanics and Mining Sciences, v. 41, p. 426.

Labaume, P., J. F. Ritz, and H. Philip, 1989, Failles normales récentes dans les Alpes sud-occidentales: Leurs relations avec la tectonique compressive: Comptes Rendus de l'Académie des Sciences, v. 308, p. 1553–1560.

Labaume, P., M. Jolivet, F. Souquière, and A. Chauvet, 2008, Tectonic control on diagenesis in a foreland basin: Combined petrologic and thermochronologic approaches in the Grès d'Annot basin (late Eocene–early Oligocene, French-Italian external Alps): Terra Nova, v. 20, p. 95–101, doi:10.1111/j.1365-3121.2008.00793.x.

Labaume, P., et al., 2009, Diagenesis controlled by tectonic burial in a foreland basin turbidite formation: The case example of the Grès d'Annot, French-Italian external Alps: Geophysical Research Abstracts, European Geosciences Union General Assembly 2009, Vienna, Austria, April 19–24, 2009, v. 11.

Lander, H. R., R. E. Larese, and L. M. Bonnell, 2008, Toward more accurate quartz cement models: The importance of euhedral versus noneuhedral growth rates: AAPG Bulletin, v. 92, no. 11, p. 1537–1563, doi:10.1306/07160808037.

Laubach, S. E., 2003, Practical approaches to identifying sealed and open fractures: AAPG Bulletin, v. 87, p. 561–579, doi:10.1306/11060201106.

Laubach, S. E., and M. E. Ward, 2006, Diagenesis in porosity evoulution of opening-mode fractures, Middle Triassic to Lower Jurassic La Boca Formation, NE Mexico: Tectonophysics, v. 419, p. 75–97, doi:10.1016/j.tecto.2006.03.020.

Laubach, S. E., P. Eichhubl, C. Hilgers, and R. H. Lander, 2010, Structural diagenesis: Journal of Structural Geology, v. 32, p. 1866–1872, doi:10.1016/j.jsg.2010.10.001.

Leclère, H., M. Buatier, D. Charpentier, J.-P. Sizun, P. Labaume, and T. Cavailhes, 2012, Formation of phyllosilicates in a fault zone affecting deeply buried arkosic sandstones: Their influence on fault zone petrophysic properties (Annot sandstones, French, external Alps): Swiss Journal of Geosciences, v. 105, p. 299–312, doi:10.1007/s00015-012-0099-z.

Mertz, J.-D., 1991, Structures de porosité et propriétés de transport dans les grès: Ph.D. thesis, Université de Strasbourg, Strasbourg, France, 129 p.

Monicard, R., 1975, Cours de production: Caractérisation des roches réservoirs, analyse de carottes: Institut Français du Pétrole Publication: Paris, France, Editions Technip, 203 p.

Mullis, J., K. M. Rahn, P. Schwer, C. Capitani, W. B. Stern, and M. Frey, 2002, Correlation of fluid inclusion temperatures with illite "crystallinity" data and clay mineral chemistry in sedimentary rocks from the external part of the central Alps: Schweizerische Mineralogische und Petrographische Mitteilung, v. 82, p. 325–340.

Olson, J. E., S. E. Laubach, and R. H. Lander, 2009, Natural fracture characterization in tight-gas sandstones: Integrating mechanics and diagenesis: AAPG Bulletin, v. 93, p. 1535–1549, doi:10.1306/08110909100.

Passchier, C. W., and R. A. J. Trouw, 2005, Microtectonics: Berlin, Germany, Springer, p. 1–366.

Philip, Z. G., J. W. Jennings, J. E. Olson, S. E. Laubach, and J. Holder, 2005, Modeling coupled fracture-matrix fluid flow in geomechanically simulated fracture networks: Society of Petroleum Engineers Journal, v. 21, p. 658–662.

Pochat, S., and J. van den Driessche, 2007, Impact of syn-sedimentary metre-scale normal fault scarps on sediment gravity flow dynamics: An example from the Grès d'Annot Formation, SE France: Sedimentary Geology, v. 202, p. 796–820, doi:10.1016/j.sedgeo.2007.09.005.

Ramsay, J. G., 1967, Folding and fracturing of rocks: New York, McGraw-Hill Book Company, p. 1–560.

Renard, F., and P. Ortoleva, 1997, Pressure solution in sandstones: Influence of clays and dependence on temperature and stress: Tectonophysics, v. 280, p. 257–266, doi:10.1016/S0040-1951(97)00039-5.

Richard, J., and J.-P. Sizun, 2011, Pressure solution-fracturing interactions in weakly cohesive carbonate sediments and rocks: Example of the synsedimentary deformation of the Campanian chalk from the Mons Basin (Belgium): Journal of Structural Geology, v. 33, no. 2, p. 154–168, doi:10.1016/j.jsg.2010.11.006.

Riepe, L., S. Wachs, and J. R. Schopper, 1983, Pressure effect on permeability: Transactions of the 8th European Formation Evaluation Symposium of the Society of Petrophysicists and Well Log Analysts, London, United Kingdom, Paper B, March 1983, p. 1–24.

Rushing, J .A., K. E. Newsham, P. M. Lasswell, J. C. Cox, and T. A. Blasingame, 2004, Klinkenberg-corrected

permeability measurements in tight-gas sands: Steady-state versus unsteady-state techniques: Society of Petroleum Engineers Annual Technical Conference and Exhibition, Houston, Texas, SPE Paper 89867, September, p. 1–11.

Sanchez, G., 2010, Chronologies et évolution de la déformation de la croûte moyenne à la surface dans un prisme collisionel en décrochement: Impacts sur l'aléa sismo-gravitaire—Exemple des Alpes sud-occidentales, France: Ph.D. thesis, Nice-Sophia Antipolis University, Nice, France, 294 p.

Sigda, M. J., and J. L. Wilson, 2003, Are faults preferential flow paths through semiarid and arid vadose zones: Water Resources Research, v. 39, p. 1225.

Surma, F., Y. Géraud, L. Pourcelot, F. Gauthier-Lafaye, J. B. Clavaud, M. Zamora, M. Lespinasse, and M. Cathelineau, 2003, Porosity microstructures of a sandstone affected by a normal fault: Bulletin de la Société Géologique de France, v. 174, no. 3, p. 295–303, doi:10.2113/174.3.295.

Vidal, O., T. Parra, and F. Trotet, 2001, A thermodynamic model for Fe-Mg aluminous chlorite using data from phase equilibrium experiments and natural pelitic assemblages in the 100.600°C, 1.25 kbar range: American Journal of Science, v. 301, no. 6, p. 557–592, doi:10.2475/ajs.301.6.557.

Ward, M. E., S. E. Laubach, and R. Marrett, 2006, Testing the use of microfractures to predict fracture orientation and intensity, La Boca Formation, northeast Mexico: AAPG 2006 Annual Convention Abstracts, v. 15, p. 112.

Wibberley, C. A. J., 1999, Are feldspar-to-mica reactions necessarily reaction softening processes in fault zones?: Journal of Structural Geology, v. 21, p. 1219–1227, doi:10.1016/S0191-8141(99)00019-X.

Zinsner, B., and F. M. Pellerin, 2007, A geoscientist's guide to petrophysics: Paris, France, Editions Technip, 450 p.